


RESEARCH ARTICLE | JUNE 20 2024

# A silicon photonics waveguide-coupled colloidal quantum dot photodiode sensitive beyond 1.6 $\mu\text{m}$

Special Collection: [Mid-IR Photonics](#)

Chao Pang ; Yu-hao Deng ; Ezat Kheradmand; Luis Moreno Hagelsieb ; Yujie Guo; David Cheyns; Pieter Geiregat ; Zeger Hens ; Dries Van Thourhout 

 Check for updates

*APL Photonics* 9, 066113 (2024)  
<https://doi.org/10.1063/5.0206386>



## Articles You May Be Interested In

Generalized weighted statistical convergence in non-archimedean fields

*AIP Conf. Proc.* (June 2019)

Scaling up silicon photonic-based accelerators: Challenges and opportunities

*APL Photonics* (February 2022)

Comparative performance of fluorite-structured materials for nanosupercapacitor applications

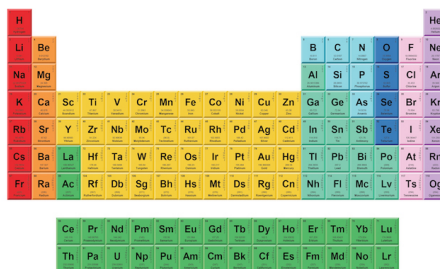
*APL Mater.* (July 2024)

29 November 2024 08:07:09



THE MATERIALS SCIENCE MANUFACTURER®

**Now Invent.™**



American Elements  
 Opens a World of Possibilities

...Now Invent!

[www.americanelements.com](http://www.americanelements.com)

© 2021-2024 American Elements & U.S. Registered Trademark

# A silicon photonics waveguide-coupled colloidal quantum dot photodiode sensitive beyond 1.6 $\mu\text{m}$

Cite as: APL Photon. 9, 066113 (2024); doi: 10.1063/5.0206386

Submitted: 1 March 2024 • Accepted: 6 June 2024 •

Published Online: 20 June 2024



View Online



Export Citation



CrossMark

Chao Pang,<sup>1,2,3,a)</sup> Yu-hao Deng,<sup>2,3</sup> Ezat Kheradmand,<sup>2,3</sup> Luis Moreno Hagelsieb,<sup>4</sup> Yujie Guo,<sup>1,2</sup>   
David Cheyns,<sup>4</sup> Pieter Geiregat,<sup>2,3</sup> Zeger Hens,<sup>2,3</sup> and Dries Van Thourhout<sup>1,2</sup>

## AFFILIATIONS

<sup>1</sup> Photonics Research Group, Ghent University - IMEC, 9052 Gent, Belgium

<sup>2</sup> NB Photonics, Ghent University, 9052 Gent, Belgium

<sup>3</sup> Physics and Chemistry of Nanostructures Group, Ghent University, 9000 Gent, Belgium

<sup>4</sup> IMEC, 3001 Leuven, Belgium

**Note:** This paper is part of the APL Photonics Special Topic on Mid-IR Photonics.

<sup>a)</sup> Author to whom correspondence should be addressed: [Chao.Pang@UGent.be](mailto:Chao.Pang@UGent.be)

## ABSTRACT

Silicon photonics faces a persistent challenge in extending photodetection capabilities beyond the 1.6  $\mu\text{m}$  wavelength range, primarily due to the lack of appropriate epitaxial materials. Colloidal quantum dots present a promising solution here, offering distinct advantages, such as infrared wavelength tunability, cost-effectiveness, and facile deposition. Their unique properties position them as a potential candidate for enabling photodetection in silicon photonics beyond the conventional telecom wavelength, thereby expanding the potential applications and capabilities within this domain. In this study, we have successfully integrated lead sulfide (PbS) colloidal quantum dot photodiodes (QDPDs) onto silicon waveguides using standard process techniques. The integrated photodiodes exhibit a remarkable responsivity of 1.3 A/W (with an external quantum efficiency of 74.8%) at a wavelength of 2.1  $\mu\text{m}$ , a low dark current of only 106 nA, and a bandwidth of 1.1 MHz under a  $-3$  V bias. To demonstrate the scalability of our integration approach, we have developed a compact 8-channel spectrometer incorporating an array of QDPDs. This achievement marks a significant step toward realizing a cost-effective photodetector solution for silicon photonics, particularly tailored for a wide range of sensing applications around the 2  $\mu\text{m}$  wavelength range.

© 2024 Author(s). All article content, except where otherwise noted, is licensed under a Creative Commons Attribution (CC BY) license (<https://creativecommons.org/licenses/by/4.0/>). <https://doi.org/10.1063/5.0206386>

## I. INTRODUCTION

Silicon photonics is renowned for its capability to miniaturize complex bulk systems into cost-effective and robust chips, finding applications in fields ranging from data/telecommunications to sensing.<sup>1–3</sup> Despite the widespread use of silicon photonics, current applications predominantly use light with wavelengths shorter than 1.6  $\mu\text{m}$ . This limitation is not a choice. Numerous applications, including environmental monitoring, medical diagnostics, and industrial sensing, would profit from photonic chips operating at longer wavelengths.<sup>4,5</sup> Such applications are, however, hampered by the lack of a scalable and cost-effective integrated technology for photodetection beyond 1.6  $\mu\text{m}$ .

Different strategies are being explored to extend the photodetection wavelength range of silicon photonics. A commonly used technique involves wafer or die bonding of III–V materi-

als, typically GaSb-based compounds, onto silicon.<sup>6–9</sup> However, this method requires large-area planarized surfaces and relies on costly III–V epitaxy and bonding technology. In addition, two-dimensional (2D) materials, such as graphene and black phosphorus, are extensively investigated for on-chip photodetection beyond 1.6  $\mu\text{m}$ .<sup>10</sup> The promise of these materials lies in the favorable substrate compatibility and broad absorption range, yet scalability poses a substantial hurdle for the practical integration of 2D photodetectors. Moreover, the performance of these photodetectors needs further improvement, for example, to enhance dark current performance and responsivity.<sup>11,12</sup> Alternatively, the direct deposition on Si of GeSn alloys,<sup>13–16</sup> III–V quantum dots,<sup>17</sup> or poly-crystalline tellurium thin films<sup>18</sup> can result in cost-effective photodetectors with straightforward fabrication processes. However, the current implementations of these methods result in photodetectors with high dark current and low responsivity, necessitating further development.

To address the challenge of cost-effective photodetection beyond the telecom range in silicon photonics, colloidal quantum dots (QDs) offer a promising solution. First of all, QDs have economical advantage in both material synthesis and deposition processes. Synthesized through wet-chemical methods, they exhibit significantly lower material cost (10\$ to 60\$ per gram<sup>19</sup>) and can be deposited as thin films on 200 mm silicon wafers through, for example, spin-coating or spray coating. The excellent compatibility of QDs with various substrates makes QDs particularly well-suited for heterogeneous material integration, in stark contrast with more traditional III–V epitaxial semiconductors. Moreover, the absorption spectrum of QDs can be readily tuned across the infrared by adjusting the QD size and utilizing different materials. Photodetectors made from PbS,<sup>20–23</sup> HgTe,<sup>24,25</sup> Ag<sub>2</sub>Se,<sup>26,27</sup> or InAs<sup>28</sup> QDs have all shown sensitivity for short-wave and mid-wave infrared light.

Given the appealing features of QDs, interest is growing in integrating QD-based emitters and detectors on photonic chips. In particular for visible light, electrically pumped light-emitting devices and optically pumped lasers have been demonstrated by combining CdSe-based QDs with silicon nitride (SiN) photonic chips.<sup>29–33</sup> More recently, waveguide-coupled QD-based photodiodes operating at around 1.3  $\mu\text{m}$  were demonstrated on the same SiN platform. This achievement underscored the potential of QDs as scalable photodetectors within photonic integrated circuits (PICs).<sup>34</sup> For wavelengths beyond 1.6  $\mu\text{m}$ , recent developments include the demonstration of plasmonic HgTe-based photoconductors on silicon waveguides<sup>35</sup> operating at 2.3  $\mu\text{m}$  with a responsivity of 23 mA/W. On the other hand, PbS QD-based photodiodes (QDPDs) sensitive up to 2.1  $\mu\text{m}$  with a responsivity of 0.385 A/W were achieved by sandwiching the QD film between a NiO p-type and a ZnO n-type contact.<sup>36</sup> Such reports point toward the promise of using integrated QDPDs for photodetection beyond 1.6  $\mu\text{m}$ , provided that low dark currents and high responsivity can be realized in integration-ready QDPD stacks.

In this work, we report on a silicon photonics, waveguide-coupled QD photodiode (WG-QDPD) that features a spectral response extending beyond 1.6  $\mu\text{m}$ . Leveraging an optimized QDPD design and a proven process flow,<sup>34</sup> we demonstrate WG-QDPDs exhibiting a responsivity of 1.3 A/W at 2.1  $\mu\text{m}$ , a low dark current of 106 nA, and a bandwidth of 1.1 MHz. Moreover, we show that our WG-QDPD exhibits a low noise equivalent power (NEP) of 0.15 pW/ $\sqrt{\text{Hz}}$  due to its high responsivity and low dark current, which is attractive for low-noise, weak signal detection. We demonstrate the reliability of the integration approach by realizing a compact on-chip spectrometer that features an array of 8 WG-QDPDs and operates in the spectral window between 2.063 and 2.135  $\mu\text{m}$ .

## II. RESULTS AND DISCUSSION

### A. QDPDs with wavelength response up to 2.1 $\mu\text{m}$

Before integrating QDPDs on waveguides, we optimized the material stack using dummy surface-illuminated QDPDs fabricated on glass-ITO substrates. Our approach involved adapting the p-i-n structure developed to form 1.3  $\mu\text{m}$  WG-QDPDs for PbS QDs with a bandgap transition at 2.1  $\mu\text{m}$ .<sup>34</sup> All the PbS QDs were synthesized by reacting lead oleate with a substituted thiourea, where different QD sizes were obtained by using differently substituted thioureas in

agreement with the literature.<sup>37</sup> The resulting PbS QDs have a surface terminated by lead oleate. More details on the synthesis and the material characteristics can be found in the Appendix A.

As shown in Fig. 1(a), we made QDPD stacks consisting of a 100 nm thick ITO transparent bottom electrode, a 30 nm thick sol-gel ZnO film functioning as an electron transport and hole blocking layer, a multilayer QD stack, and an Au top electrode. Within the QD film, the photosensitive layer consisted of QDs with a bandgap transition at 2.1  $\mu\text{m}$  (Appendix A, Fig. 7). In a first design [structure A in Fig. 1(a)], this film—formed by spin coating—was exposed to a methanol solution containing 10 mg/ml tetra-n-butylammonium iodide (TBAI) for 30 s. This process removes the as-synthesized surface ligands, thereby turning the QD film n-type and enhancing the electron mobility. As the hole transport and electron blocking layer, we employed a film of PbS QDs featuring a 0.94  $\mu\text{m}$  bandgap transition. This film was similarly exposed to a 0.01 vol% ethanedithiol (EDT) in a methanol solution, which leads to p-type doping,<sup>38,39</sup> and a gold contact was evaporated on top. However, as shown in Fig. 1(b) (red line), this stack showed little rectification, and a dark current density of nearly 10 mA/cm<sup>2</sup> at  $-2$  V reverse bias, which is more than two orders higher than QDPDs using PbS QDs with 1.3  $\mu\text{m}$  bandgap transition as photosensitive layers (Appendix B, Fig. 8). In an attempt to reduce the dark current, we explored two additional QDPD stacks; a first in which the film of 2.1  $\mu\text{m}$  PbS QDs was sandwiched between layers of 1.3  $\mu\text{m}$  PbS QDs, which we also treated using TBAI and a second where the 1.3  $\mu\text{m}$  PbS QDs were only included between the 2.1 and 0.94  $\mu\text{m}$  PbS QD films, as shown in structure B and C in Fig. 1(a). Interestingly, structure B showed a strongly enhanced rectification and a 10-fold reduction in the dark current as compared to the initial stack, while structure C only featured a minor reduction in the dark current. This difference indicates that the primary source of dark current is the leakage of charge carriers between the 2.1  $\mu\text{m}$  PbS QDs and the ZnO contact, possibly assisted through trap states at the ZnO surface,<sup>20</sup> for which the 1.3  $\mu\text{m}$  PbS QD film provides an additional barrier.

The optimized QDPD with structure B was characterized with a 2.1  $\mu\text{m}$  laser that had a power of 870  $\mu\text{W}$  and a peak power density of 220 mW/cm<sup>2</sup>. Under a  $-3$  V bias, the QDPD shows a dark current of 50.3  $\mu\text{A}$  (dark current density of 2.8 mA/cm<sup>2</sup> for a device area of 1.77 mm<sup>2</sup>) and a responsivity of 0.19 A/W (external quantum efficiency, EQE, of 11.2%), as shown in Fig. 1(c). This relatively low EQE probably reflects the limited absorption of the vertically incident light in the thin layer of 2.1  $\mu\text{m}$  PbS QDs and the relatively low transmittance of ITO at 2.1  $\mu\text{m}$ .<sup>36</sup> The 1.3  $\mu\text{m}$  PbS-TBAI layer between the 2.1  $\mu\text{m}$  PbS-TBAI and PbS-EDT layers should be n-doped,<sup>38</sup> posing challenges for hole transport and potentially leading to an increase in the series resistance of the QDPD. However, the I–V characteristics at forward bias did not show degradation compared to structure A [Fig. 1(b)]. Possibly, this layer is turned into p-type during the subsequent EDT ligand exchange process for the 0.94  $\mu\text{m}$  PbS QD layer on top. EDT, known for its high reactivity compared to TBAI,<sup>40</sup> can soak the 1.3  $\mu\text{m}$  PbS-TBAI layer underneath, resulting in a change of doping to p-type. To validate this hypothesis, QDPDs with structure B were fabricated, but the ligand exchange of the top 1.3  $\mu\text{m}$  PbS QDs was altered to EDT instead of TBAI. QDPDs with either TBAI or EDT ligand exchange on the 1.3  $\mu\text{m}$  QDs exhibited nearly identical dark and light I–V characteristics (Appendix B, Fig. 9), thus confirming our above-mentioned

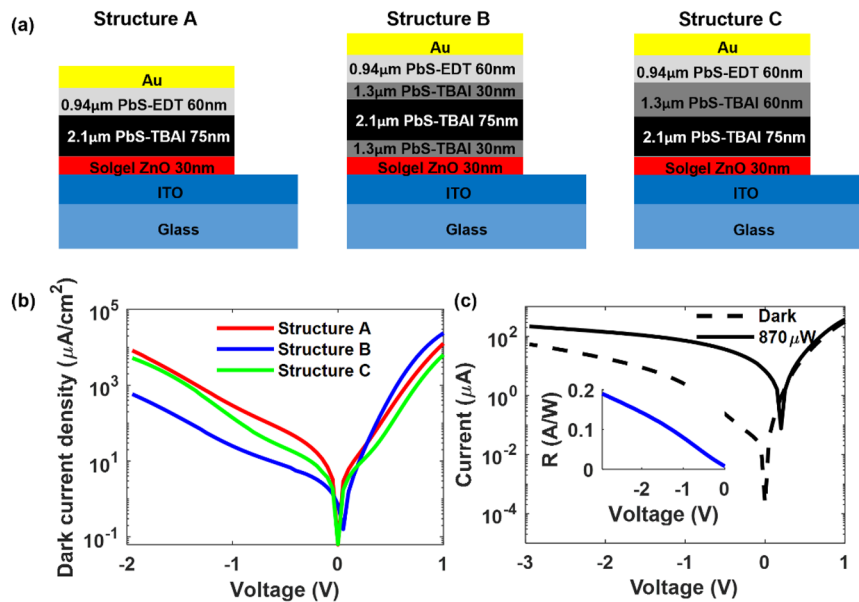


**FIG. 1.** Structure and characterization of QDPD. (a) Vertical QDPD structures with surface illumination. (b) Influence of the interface layer on dark current density. (c) Dark current and photocurrent of structure B QDPD, with an area of  $1.77 \text{ mm}^2$ . The photocurrent was measured with a  $2.1 \text{ }\mu\text{m}$  laser Gaussian beam illuminated from the bottom glass side, with a peak power density of  $220 \text{ mW/cm}^2$ . Inset: responsivity of QDPD vs bias voltage.

assumption. The spectral response of the QDPD with structure B was measured by sweeping the laser wavelength, showing a photo response extending up to  $2.2 \text{ }\mu\text{m}$  (Appendix B, Fig. 10), consistent with the absorption spectrum of the QDs. More details regarding the fabrication of the QDPD are given in Appendix C.

## B. Integration of QDPDs on waveguides

Figures 2(a)–2(e) show the process flow used to integrate the QDPD on waveguides. In a first step, waveguides were defined on silicon-on-insulator (SOI) substrates with a  $2 \text{ }\mu\text{m}$  buried oxide and a  $220 \text{ nm}$  silicon layer, employing a  $70 \text{ nm}$  shallow etch. To alleviate the power saturation problem of WG-QDPDs, as observed in a previous demonstration at a shorter wavelength on the SiN platform,<sup>34</sup> we defined  $30 \text{ }\mu\text{m}$  wide waveguides. This adjustment serves to lower the optical power density in the QD film. Next, the waveguide was planarized by flowable oxide (hydrogen silsesquioxane, HSQ), followed by annealing at  $400 \text{ }^\circ\text{C}$  in  $\text{N}_2$  to increase the physical and chemical stability of HSQ. This step resulted in a  $45 \text{ nm}$  top cladding on the waveguides, shown in light blue in Fig. 2(a). As shown in Figs. 2(b)–2(e), the QDPD stack was then integrated on top, starting with the sputtering of an  $18 \text{ nm}$  thick ITO layer as the bottom electrode. The ITO had a sheet resistance of  $173 \text{ }\Omega/\square$ , and the layer thickness was reduced as compared to the dummy surface-illuminated QDPD structure in order to minimize optical losses in the ITO and maximize light absorption in the PbS QD film. To further reduce optical loss, the ITO layer was restricted to the designated area for photodetection using HCl-based wet etching. Next, we deposited the ZnO layer using sol-gel chemistry and patterned it using a dilute HCl solution. Complete coverage of ITO with ZnO is crucial to prevent direct contact between ITO and the

subsequently deposited QD film, as this could lead to a significant leakage current. Ti/Au ( $20 \text{ nm}/100 \text{ nm}$ ) was placed on the side of the waveguides as the n-contact pad using a lift-off technique. The same QD stacks with structure B, as we used in the surface-illuminated QDPD, were deposited layer by layer and lifted off simultaneously to achieve the desired pattern. PMMA resist was used for its excellent chemical compatibility with the methanol solvent involved during QDs deposition. Finally,  $80 \text{ nm}$  Au was deposited on top as p-contact pads through thermal evaporation and lift-off. The cross section of the fabricated WG-QDPD is shown in Fig. 2(f). More details on the integration process are given in Appendix D.

## C. Characterization of WG-QDPD

We characterized the WG-QDPDs using a  $2.1 \text{ }\mu\text{m}$  laser, employing grating couplers for convenient light coupling into and out of the waveguide. The optical power in the waveguide was calibrated by measuring the coupling efficiency of the grating coupler for a reference waveguide without QDPDs. The WG-QDPD showed a dark current of  $106 \text{ nA}$  at  $-3 \text{ V}$ , as shown in Fig. 3(a). Considering a WG-QDPD width of  $30 \text{ }\mu\text{m}$  and a length of  $200 \text{ }\mu\text{m}$ , the dark current density ( $1.8 \text{ mA/cm}^2$ ) is in line with the measurements obtained on the surface-illuminated QDPDs ( $2.8 \text{ mA/cm}^2$ ), indicating that the integration process does not introduce spurious leakage paths. The responsivity reaches  $1.3 \text{ A/W}$  (EQE of  $74.8\%$ ) at an optical power of  $116 \text{ nW}$ , as shown in Fig. 3(b). The significantly higher EQE compared to surface-illuminated QDPDs is attributed to increased absorption during propagation within the waveguides. For WG-QDPDs, the Si and QD stack constitute the hybrid waveguide designed for the propagation of the fundamental TE mode. Light is absorbed via the evanescent tail of the optical

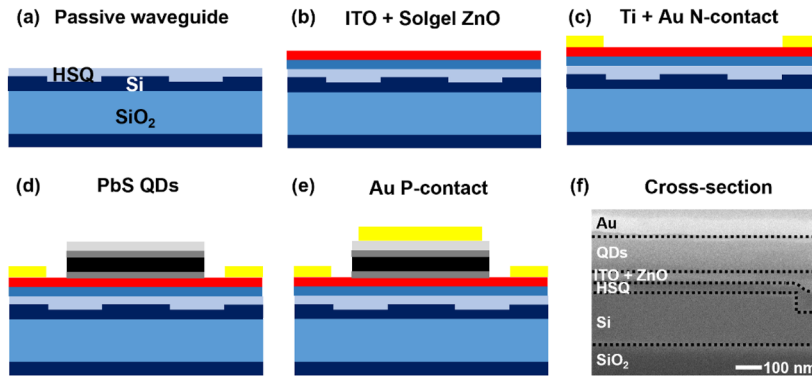


**FIG. 2.** Integration steps to fabricate WG-QDPD. (a) Si rib waveguide patterning and planarization. (b) ITO sputtering and patterning with wet etching, followed by ZnO deposition with the sol-gel method and patterning with wet etching. (c) N-contact metal patterning with lift-off. (d) QD film patterning with PMMA resist and lift-off. (e) P-contact metal patterning with PMMA resist and lift-off. (f) Cross section of the fabricated WG-QDPD.

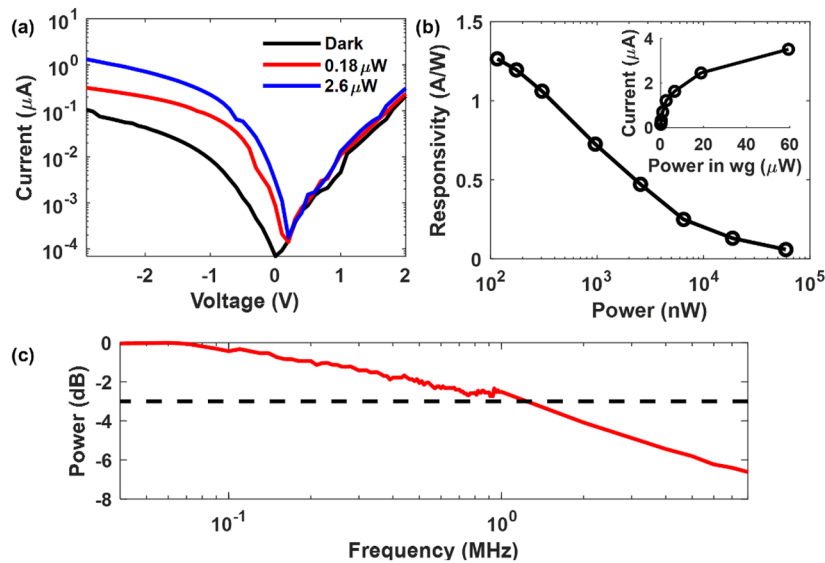


**FIG. 3.** Response of WG-QDPDs. (a) I–V curves of WG-QDPDs under a dark condition and illumination at 2.1  $\mu\text{m}$ . (b) Responsivity vs optical power at  $-3\text{ V}$  bias voltage. Inset: photocurrent vs optical power. (c) Bandwidth of the integrated WG-QDPD.

mode during its propagation, as depicted in Appendix D, Fig. 11. In contrast to surface-illuminated QDPDs, which require a thick QD absorption layer for efficient light absorption, the extended absorption path of guided light in WG-QDPDs ensures efficient absorption even with a thin layer of QD. The combination of low dark current and high responsivity leads to a low estimated noise equivalent power ( $\text{NEP} = \sqrt{2I_{\text{dark}}q}/R$ , where  $q$  is the elementary charge and  $R$  is the responsivity) of  $0.15\text{ pW}/\sqrt{\text{Hz}}$ , indicating that WG-QDPDs are well-suited for weak signal detection. The photocurrent exhibits nonlinear growth with optical power, a phenomenon attributed to QDPD saturation due to high series resistance, as observed in prior studies.<sup>34</sup>

The speed of the fabricated WG-QDPD was measured at  $1.55\text{ }\mu\text{m}$ , exhibiting a bandwidth of  $1.1\text{ MHz}$ , as shown in Fig. 3(c).

Under a large reverse bias of  $-3\text{ V}$ , the thin QD absorption layer can be considered completely depleted.<sup>41</sup> Therefore, the response time ( $\tau_{\text{res}}$ ) of the photodetector is determined by the drift progress ( $\tau_{\text{drift}}$ ) and the resistance–capacitance constant ( $\tau_{\text{RC}}$ ) of the electrical circuit  $\tau_{\text{res}} = \sqrt{\tau_{\text{drift}}^2 + (2.2\tau_{\text{RC}})^2}$ .<sup>42</sup> The drift time  $\tau_{\text{drift}}$  is governed by the carrier mobility ( $\mu$ ) and the voltage drop ( $V$ ) across the depleted film thickness ( $d$ ), with  $\tau_{\text{drift}} = \frac{d^2}{\mu V}$ . The other term,  $\tau_{\text{RC}} = RC$ , where  $R$  represents the series resistance and  $C$  denotes the capacitance. For a fully depleted QDPD, we estimate the series resistance  $R$  using the access resistance (ITO sheet resistance and contact resistance between n-contact and ZnO), measured to be  $\sim 100\text{ }\Omega$  for our WG-QDPDs. The capacitance  $C$  is estimated to be around  $4.1\text{ pF}$  ( $C = \frac{\epsilon_0 \epsilon_r A}{d}$ , where  $\epsilon_0$  represents the vacuum permittivity,  $\epsilon_r = 15.5$

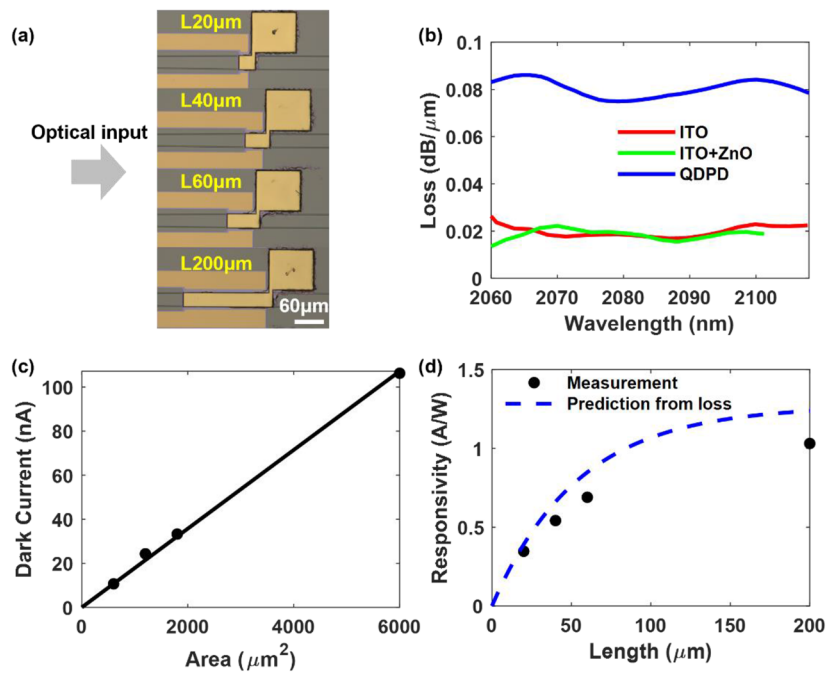


**FIG. 4.** Performance of WG-QDPDs with different lengths. (a) Top view of WG-QDPDs. (b) Optical absorption resulting from materials integrated onto waveguides. The measurements were obtained through optical transmission, with varying lengths for each material. (c) Dark current of devices with different area. (d) Responsivity of WG-QDPDs with different lengths. The predicted relationship between responsivity and length is presented by a dashed blue line, derived from the optical loss measurements shown in Fig. 4(b).

denotes the dielectric constant of the PbS-QD film,<sup>41</sup>  $A = 6000 \mu\text{m}^2$  is the area of QDPD, and  $d = 195 \text{ nm}$  is the thickness of the PbS QD film). The estimated  $\tau_{RC}$  is 0.41 ns, corresponding to a BW of 388 MHz using the relationship,  $\text{BW} = 0.35/\tau_{res}$ .<sup>42</sup> Considering a measured BW of 1.1 MHz, the speed of our WG-QDPD is likely drift-limited. Furthermore, we measured the BW of WG-QDPDs with areas of 6000 and 600  $\mu\text{m}^2$ , both exhibiting similar bandwidths (see Appendix E, Fig. 13). This area-insensitive BW is contrary to the scenario where  $\tau_{RC}$  dominates the speed of QDPDs,<sup>23,41</sup> considering a consistent series resistance and area-related capacitance. This drift-limit speed can be further supported by examining  $\tau_{drift}$ . The carrier mobility of the 2.1  $\mu\text{m}$  PbS-TBAI absorption layer, extracted via the field effect transistor (FET) measurements,<sup>41</sup> is  $(0.94 \pm 0.6) \times 10^{-4} \text{ cm}^2 \text{ V}^{-1} \text{ s}^{-1}$  for electrons and  $(1.41 \pm 0.35) \times 10^{-4} \text{ cm}^2 \text{ V}^{-1} \text{ s}^{-1}$  for holes. Considering a thickness of 75 nm for the absorption layer and a voltage drop of 3 V, the estimated  $\tau_{drift}$  is around 0.2  $\mu\text{s}$ , corresponding to a bandwidth of 1.75 MHz. The carrier transition time in the 1.3  $\mu\text{m}$  PbS-TBAI and 0.94  $\mu\text{m}$  PbS-EDT layers is disregarded due to the significantly faster carrier mobilities exceeding  $1 \times 10^{-3} \text{ cm}^2 \text{ V}^{-1} \text{ s}^{-1}$  in both layers.<sup>41</sup> Although the bandwidth of our demonstrated WG-QDPDs may not be as high as that of III-V photodiodes, it meets the requirements of many sensing applications. Further improvement on the speed of the WG-QDPD relies on improved ligand exchange strategies to boost the mobility of the 2.1  $\mu\text{m}$  PbS QD layer. Reducing the thickness of the QD film can also decrease  $\tau_{drift}$ . This strategy was recently adopted to achieve QDPDs

with a response time of 4 ns.<sup>41</sup> More details on the characterization of WG-QDPDs are given in Appendix E.

On the same chip, we incorporated WG-QDPDs with varying lengths, as shown in Fig. 4(a). We conducted transmission measurements on the waveguides after patterning each material. These measurements allowed us to ascertain the optical loss induced by each material, as shown in Fig. 4(b). The ITO layer introduced an optical loss of around 0.02 dB/ $\mu\text{m}$ , resulting from strong free carrier absorption in the infrared.<sup>43</sup> The addition of the ZnO layer did not introduce measurable extra absorption. The entire QDPD stack raised the optical loss to 0.08 dB/ $\mu\text{m}$ , indicating that the absorption is dominated by the QD film. This strong absorption competes with the absorption from the ITO bottom electrode, ensuring high responsivity of our WG-QDPDs. The dark current of these WG-QDPDs is proportional to the area, with a slope of 1.8 mA/ $\text{cm}^2$ , as shown in Fig. 4(c). The responsivity of WG-QDPDs, measured at  $-3 \text{ V}$  bias and 400 nW optical power, shows a saturation behavior with respect to the PD length, as shown in Fig. 4(d). The saturation behavior aligns with the prediction from optical loss measurements, as indicated by the blue dashed line shown in Fig. 4(d).

We also investigated WG-QDPDs with different shapes, as shown in Fig. 5(a). As we mentioned before, the waveguide width is extended to 30  $\mu\text{m}$  to alleviate the optical power saturation, ensuring an efficient responsivity. However, this strategy also increases the dark current due to the larger WG-QDPD area. Consequently, the NEP exhibits a trade-off between responsivity and dark current.

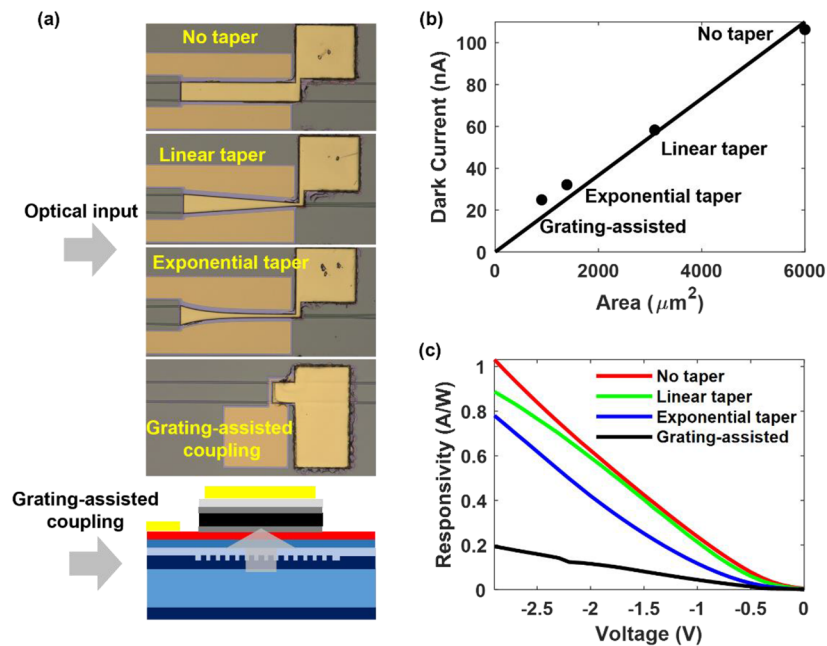


**FIG. 5.** Performance of WG-QDPDs with different shapes. (a) Top view of WG-QDPDs. Light is coupled into waveguides from the left side. (b) Dark current of different WG-QDPDs. (c) Responsivity of different WG-QDPDs.

Notably, heavy optical power saturation predominantly occurs in the initial section of the WG-QDPD. As light propagates within the waveguides, the optical power decreases exponentially. This insight allows us to narrow down the waveguide width at the far end without introducing significant power saturation. In our design, we implemented waveguide narrowing from 30 to 0.9  $\mu\text{m}$  using both linear and exponential tapers, while keeping a consistent length of 200  $\mu\text{m}$ . For the exponential taper, the width decreases at a rate of 0.023  $\mu\text{m}^{-1}$  (0.1 dB/ $\mu\text{m}$ ), similar to the optical absorption measurement shown in Fig. 4(b). The QDPD follows the same shape as these tapered waveguides. The linear taper reduces the WG-QDPD area to  $\sim 1/2$ , and the exponential taper further decreases the area to around  $1/3$ . Consequently, the decrease in the area reduces the dark current to  $1/2$  and  $1/3$ , respectively, as shown in Fig. 5(b). As expected, the responsivity of the tapered devices does not degrade significantly, as shown in Fig. 5(c). This results in a champion NEP of 0.13  $\text{pW}/\sqrt{\text{Hz}}$  for the exponentially tapered WG-QDPD, representing a 30% improvement compared to the NEP of the uniform WG-QDPD (0.18  $\text{pW}/\sqrt{\text{Hz}}$ ). Notably, there is an underestimation of the NEP here. The measurements were conducted at a relatively high optical power of 400 nW, which, combined with the nonlinear response to optical power, results in an underestimated responsivity.

We also fabricated a grating-assisted QDPD, where light injected from the left side was scattered vertically and absorbed by the QDPD, as shown in Fig. 5(a). This configuration yielded the lowest dark current due to the smallest QDPD size of 30  $\mu\text{m}$  by 30  $\mu\text{m}$ . However, the responsivity was significantly lower compared to the evanescent coupling scheme. The degradation in responsivity is attributed to a combined effect of upward coupling efficiency,

incomplete optical absorption in the thin QDs layer, and possibly stronger power saturation.

#### D. Demonstration of a 2.1 $\mu\text{m}$ integrated spectrometer

To demonstrate what complex tasks our proposed WG-QDPD integration approach can complete, we combined a WG-QDPD array with an eight-channel planar concave grating (PCG), forming a compact spectrometer, as shown in Fig. 6(a). The PCG, designed with IPKISS,<sup>44</sup> has a central wavelength of 2.1  $\mu\text{m}$  and a wavelength range of around 70 nm. The fabrication was carried out on the same 220 nm SOI chip alongside the aforementioned components. To simplify the fabrication process, we used 70 nm shallow-etched distributed Bragg reflectors (DBR) as retroreflectors.<sup>45</sup> FDTD simulations revealed that these DBR mirrors, with a period of 437 nm, exhibit reflection centered at 2.1  $\mu\text{m}$  (>90%) and a 3 dB bandwidth of 200 nm, meeting the PCG requirements.

The transmission spectrum of the PCG was measured prior to QDPD integration, with a tunable laser of around 2.1  $\mu\text{m}$  (IPG Cr:ZnS/Se). The fabricated PCG covers a wavelength range from 2063 to 2135 nm, with a crosstalk better than  $-20$  dB and insertion loss less than 3 dB, as shown in Fig. 6(b), consistent with design metrics.

For the WG-QDPDs, we used a width of 30  $\mu\text{m}$  and a length of 200  $\mu\text{m}$ , to obtain an efficient photo response. After integrating the WG-QDPD array, the photo-response of each channel was measured at  $-1$  V bias by sweeping the wavelength of the input laser. The

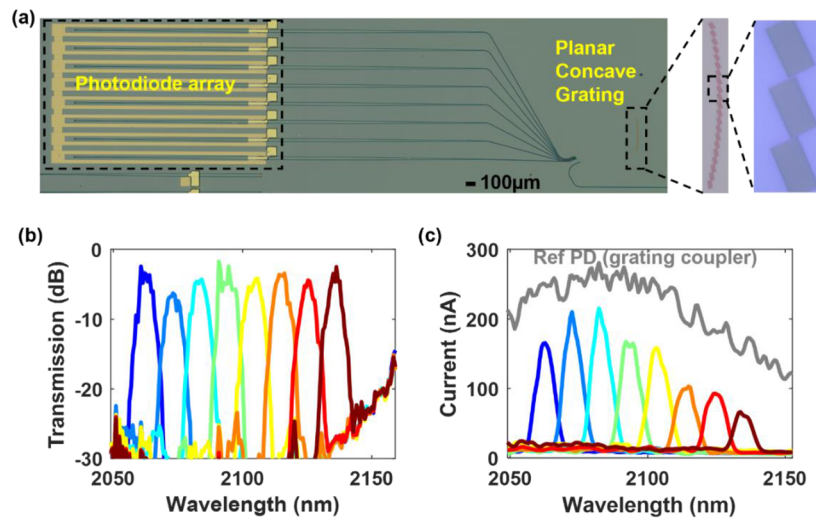


**FIG. 6.** Compact spectrometer based on a WG-QDPD array and a planar concave grating. (a) Top view of the spectrometer. Light is injected from the grating coupler on the right side. (b) Transmission spectrum of the planar concave grating. (c) Response of WG-QDPDs from eight channels and a reference waveguide (gray line).

response of the QDPD array aligns with the spectrum of the grating coupler [gray line shown in Fig. 6(c)], as measured from a reference WG-QDPD without the PCG. This consistent spectral shape indicates uniform responses of the WG-QDPDs, thereby suggesting its potential for scalable integration. The array of WG-QDPDs was measured directly without requiring further calibration. This type of spectrometer is interesting for sensing applications, such as glucose concentration monitoring.

### E. Discussion

Compared to previously reported plasmonic HgTe QD photoconductors integrated on silicon waveguides,<sup>35</sup> our integration approach achieves a similar level of dark current (106 nA), demonstrating more than one-order improvement in responsivity (1.3 A/W) and two-order improvement in bandwidth (1.1 MHz). When compared to alternative approaches for extending photodetection capabilities on the SOI platform, our proposed WG-QDPDs remain competitive in terms of dark current and responsivity. Notably, these results are on par with the best-performing bonded III–V photodetectors reported in the literature (responsivity 0.4–1.4 A/W around 2.3 μm and dark current 10 nA–2.5 μA),<sup>6–9</sup> outperforming monolithically grown GeSn (responsivity <0.52 A/W and dark current > 1 mA).<sup>15–16</sup> Another class of heterogeneous materials, 2D materials, such as graphene<sup>46</sup> or black phosphorus,<sup>47,48</sup> also possess the potential to operate beyond the telecommunication wavelength. However, they face challenges in achieving high responsivity (0.07–0.3 A/W at a wavelength of 2–3 μm)<sup>11,12,49</sup> and scalable integration. It is acknowledged that despite advancements, the bandwidth of our WG-QDPD still lags behind compared to the GHz bandwidth demonstrated by other approaches.<sup>50–52</sup> Furthermore, additional efforts are necessary to mitigate the nonlinear response of our WG-QDPD.

The performance of the WG-QDPD could be further improved by optimizing the device structure. Previous reports on QDPDs at 2.1 μm have demonstrated an impressively low dark current density of  $10^{-5}$  A/cm<sup>2</sup> and high responsivity.<sup>36</sup> Implementing such advancements could reduce the dark current of integrated photodetectors to sub-nanoampere levels, which is particularly advantageous for the detection of weak signals in sensing applications.

In addition, exploring alternative materials for long wavelength WG-QDPDs, such as HgTe<sup>25,53,54</sup> and Ag<sub>2</sub>Se,<sup>26,27</sup> is compelling to extend the photodetection capabilities within silicon photonics into the mid-infrared range, aligning with a heightened interest in sensing applications. Ag<sub>2</sub>Se QDs, which rely on intra-band absorption, is thereby the more attractive material because of the greatly reduced toxicity. However, efforts are still needed to improve the responsivity and reduce the dark current for these materials.

### III. CONCLUSION

In this work, we have demonstrated the integration of PbS QDPDs into silicon waveguides, extending the photodetection capabilities beyond the traditional telecommunication range in silicon photonics. The achieved results at room temperature, including a low dark current of 106 nA, a high responsivity of 1.3 A/W at 2.1 μm, and a bandwidth of 1.1 MHz, highlight the effectiveness of our approach. The scalability of our integration method is exemplified through the presentation of an 8-channel compact spectrometer integrated with a WG-QDPD array. This integrated system offers a promising solution for on-chip spectroscopy around 2.1 μm. We believe that QDPD technology holds significant promise for cost-effective photodetection in the near and mid-infrared ranges in silicon photonics, especially for diverse sensing applications. Future work should focus on improving the QDPD characteristics, including detectivity, bandwidth, linearity, and extending sensing wavelength range.



## ACKNOWLEDGMENTS

This work was supported by the European Research Council (ERC) under the innovation program Grant Agreement No. 884963 (ERC AdG NARIOS), the FWO-Vlaanderen for research funding (FWO Projects Nos. G0B2921N and G0C5723N), and the China Scholarship Council (CSC Grant No. 201906120023).

## AUTHOR DECLARATIONS

### Conflict of Interest

The authors have no conflicts to disclose.

### Author Contributions

**Chao Pang:** Conceptualization (lead); Data curation (lead); Formal analysis (lead); Investigation (lead); Methodology (lead); Writing – original draft (lead); Writing – review & editing (equal). **Yu-hao Deng:** Conceptualization (equal); Formal analysis (equal); Methodology (equal); Resources (equal); Writing – original draft (equal); Writing – review & editing (equal). **Ezat Kheradmand:** Formal analysis (equal); Resources (equal); Writing – original draft (equal); Writing – review & editing (equal). **Luis Moreno Hagelsieb:** Resources (equal); Writing – original draft (equal); Writing – review & editing (equal). **Yujie Guo:** Formal analysis (equal); Resources (equal); Writing – original draft (equal); Writing – review & editing (equal). **David Cheyns:** Resources (equal); Writing – original draft (equal); Writing – review & editing (equal). **Pieter Geiregat:** Funding acquisition (equal); Methodology (equal); Resources (equal); Supervision (equal); Writing – original draft (equal); Writing – review & editing (equal). **Zeger Hens:** Funding acquisition (equal); Methodology (equal); Resources (equal); Supervision (equal); Writing – original draft (equal); Writing – review & editing (equal). **Dries Van Thourhout:** Conceptualization (equal); Funding acquisition (equal); Methodology (equal); Resources (equal); Supervision (equal); Writing – original draft (equal); Writing – review & editing (equal).

### DATA AVAILABILITY

The data that support the findings of this study are available from the corresponding author upon reasonable request.

## APPENDIX A: SYNTHESIS OF MATERIALS

### 1. Synthesis of 2.1 $\mu\text{m}$ PbS QDs

Lead oleate and N-n-hexyl-N'-dodecyl thiourea were prepared according to the procedure described by Hendricks *et al.*<sup>37</sup> In a three-neck flask, 1.2 mmol lead oleate (0.9241 g) was dissolved in 20 ml n-dodecane at 150 °C under a nitrogen atmosphere. Separately, N-n-hexyl-N'-dodecylthiourea (1 mmol, 0.3286 g) was mixed with 1 ml of diglyme (diethylene glycol dimethyl ether) in a vial and heated to 150 °C. The pre-heated thiourea solution was then injected swiftly into the lead oleate solution via a syringe, and the reaction was allowed to run for 20 min at 150 °C. Subsequently, the flask was cooled down to an ambient temperature by immersion into a water bath. The final dispersion underwent four purification cycles inside a nitrogen-filled glovebox, using a solvent mixture of 4:1 toluene to

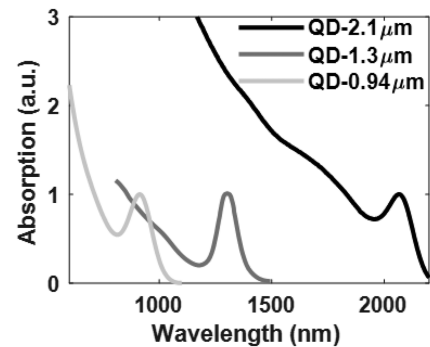


FIG. 7. Absorption spectra for three types of QD inks (dispersed in n-octane) used in QPDDs.

hexane, with methyl acetate as the non-solvent. The purified PbS QDs were dispersed in anhydrous n-octane to achieve the desired concentration.

### 2. Synthesis of 0.94 $\mu\text{m}$ PbS QDs

Lead oleate and N-[3,5-bis(trifluoromethylphenyl)]-N'-phenylthiourea were synthesized according to Hendricks *et al.*<sup>37</sup> In a three-neck flask, 7.00 mmol lead oleate (5.38 g) was dissolved in 25 ml anhydrous n-octane at 90 °C under a nitrogen atmosphere. In a vial, 4.67 mmol of N-[3,5-bis(trifluoromethylphenyl)]-N'-phenylthiourea (1.70 g, 1 eq.) and 2 ml of 1-methoxy-2-(2-methoxyethoxy)ethane were mixed and also heated to 90 °C. The thiourea solution was then quickly injected into the lead oleate solution via a syringe, and the flask was cooled down to room temperature by immersion into a water bath after one minute. The resulting dispersion was purified four times by the aid of n-octane and acetone and stored in anhydrous n-octane for further use.

### 3. Synthesis of 1.3 $\mu\text{m}$ PbS QDs

In a three-neck flask, 2 mmol lead oleate (1.54 g) was dissolved in 20 ml n-dodecane at 120 °C under a nitrogen atmosphere and flushed for 30 min. Next, 1.5 mmol of N-(p-(trifluoromethylphenyl)-N'-dodecylthiourea (0.5828 g) was mixed with 1 ml of 1-methoxy-2-(2-methoxyethoxy)ethane or diglyme under a nitrogen atmosphere, pre-heated at 120 °C, and quickly injected into the lead oleate solution at 120 °C. The reaction mixture was cooled down to room temperature by immersing the flask in a water bath after 80 s. The resulting dispersion was then purified at least four times by the aid of n-octane and acetone and stored in anhydrous n-octane for further use.

## APPENDIX B: DARK CURRENT SUPPRESSION

The structure and characterization of QPDP with 1.3 and 2.1  $\mu\text{m}$  PbS active layers. Dark current and photocurrent of QPDP with an area of 1.77 mm<sup>2</sup>. Spectral response of the QPDP with structure B, measured at a bias of -1 V and a peak power density of 220 mW/cm<sup>2</sup>.

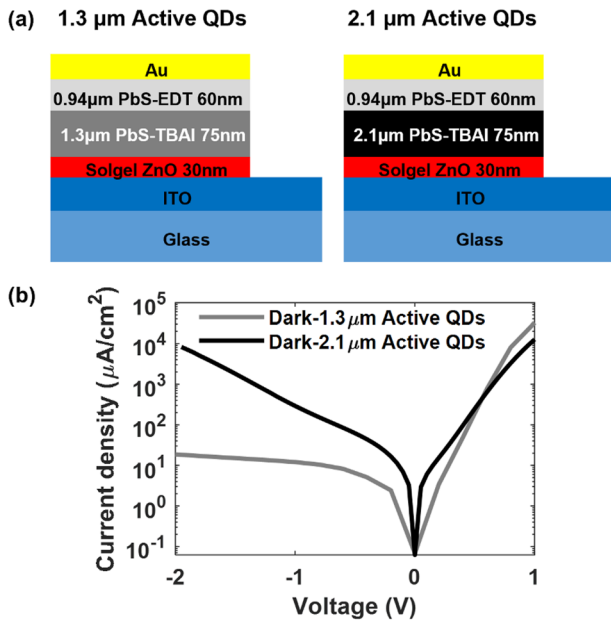


**FIG. 8.** Structure and characterization of QDPD with 1.3 and 2.1  $\mu\text{m}$  PbS active layers. (a) QDPD structures. (b) Dark current density.

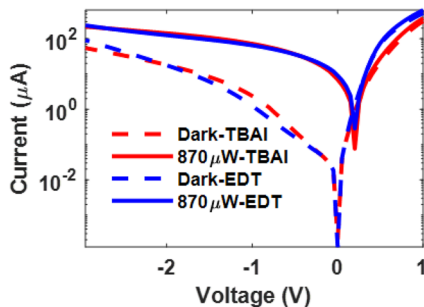


**FIG. 9.** Dark current and photocurrent of QDPD with an area of  $1.77 \text{ mm}^2$ . The photocurrent was measured with  $2.1 \mu\text{m}$  laser with a Gaussian beam illuminating the sample from the bottom glass side, with a peak power density of  $220 \text{ mW/cm}^2$ . Red: ZnO/1.3  $\mu\text{m}$ -PbS-TBAI/2.1  $\mu\text{m}$ -PbS-TBAI/1.3  $\mu\text{m}$ -PbS-TBAI/0.94  $\mu\text{m}$ -PbS-EDT. Blue: ZnO/1.3  $\mu\text{m}$ -PbS-TBAI/2.1  $\mu\text{m}$ -PbS-TBAI/1.3  $\mu\text{m}$ -PbS-EDT/0.94  $\mu\text{m}$ -PbS-EDT.

### APPENDIX C: QDPD FABRICATION

Substrates with 100 nm ITO on glass ( $2 \times 1.5 \text{ cm}^2$ , Ossila) were cleaned in acetone and isopropanol with sonication, followed by exposure to  $\text{O}_2$  plasma (PVA TePla 600) for 10 min. A 30 nm layer of ZnO was then formed on top of the ITO layer via spin-coating a precursor solution and annealing at  $325^\circ\text{C}$  for 30 min in ambient air. Following this, PbS QDs were spin-coated onto the ZnO layer, with subsequent treatment involving either 10 mg/ml tetra-n-butylammonium iodide (TBAI) in methanol or 0.01 vol % ethanedithiol (EDT) in methanol. The ligand exchange process for each cycle lasted 30 s, followed by two washes with methanol.

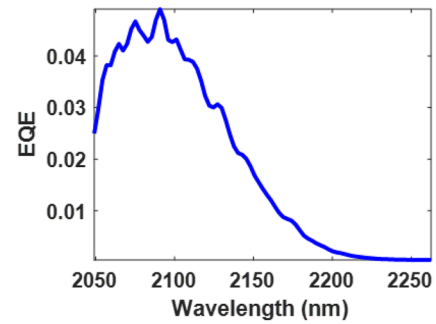


**FIG. 10.** Spectral response of the QDPD with structure B, measured at a bias of  $-1 \text{ V}$  and a peak power density of  $220 \text{ mW/cm}^2$ .

Each cycle resulted in a film with a thickness of 25 nm for 2.1  $\mu\text{m}$  PbS-TBAI, 30 nm for 1.3  $\mu\text{m}$  PbS-TBAI, and 30 nm for 0.94  $\mu\text{m}$  PbS-EDT. The QDs and ligand exchange steps were repeated multiple times to achieve the desired thickness. Finally, an 80 nm layer of gold was evaporated on top using a shadow mask, forming QDPD pixels with a diameter of 1.5 mm.

### APPENDIX D: WG-QDPD FABRICATION

#### 1. Waveguides fabrication

Waveguides were patterned with e-beam lithography (EBL) and dry etching. We used standard SOI substrates with 220 nm Si on top of 2  $\mu\text{m}$  buried oxide in this work. 400 nm ARP6200.13 e-beam resist was used as a mask, exposed by EBL (Voyager Raith 50 kV) with a dose of  $160 \mu\text{C/cm}^2$  and developed in n-amyl acetate for 60 s. The resist pattern was transferred to Si by reactive ion etching (ICP-RIE, Oxford Instruments) using  $\text{SF}_6$  and  $\text{CHF}_3$  chemistry. A 70 nm shallow etch in Si was used to define the optical structures. We then spin-coated the flowable oxide hydrogen silsesquioxane (HSQ, Dow FOX-15) on top of the sample as a top cladding layer. Diluted HSQ (HSQ: MIBK = 1:4) was spun with a speed of 4000 rpm and an acceleration of 1000 rpm/s. The sample was then cured at  $400^\circ\text{C}$  for 2 h in a nitrogen atmosphere, achieving a cladding thickness of  $\sim 45 \text{ nm}$ .

#### 2. ITO deposition and patterning

18 nm thick ITO was deposited on the sample by magnetron sputtering. Then, the ITO film was patterned with photolithography (AZ5214 E) and wet etching ( $37\% \text{ HCl:H}_2\text{O} = 1:5$ , 15 s).

#### 3. ZnO deposition and patterning

30 nm thick ZnO was deposited on the sample using the same sol-gel method outlined in Appendix C. Subsequently, the ZnO film underwent patterning through photolithography (AZ5214 E), followed by wet etching ( $37\% \text{ HCl:H}_2\text{O} = 1:1000$ , 5 s).

#### 4. N-contact deposition and patterning

The N-contact was patterned using photolithography and the lift-off method. The desired pattern was generated using AZ5214 E photoresist, followed by metal evaporation with a composition of 20 nm Ti and 100 nm Au. The sacrificial photoresist and the metal

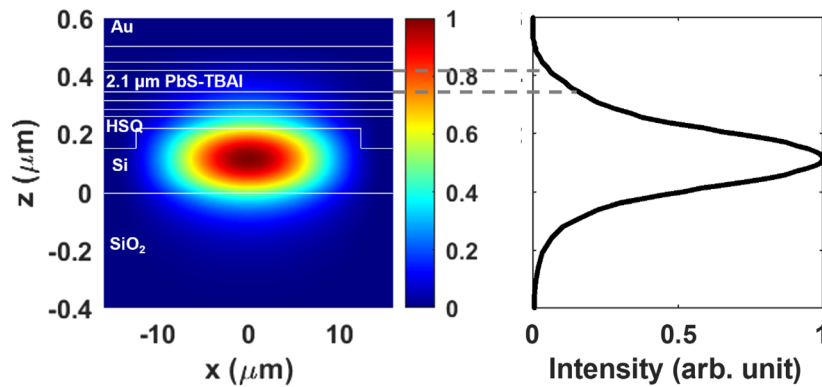


**FIG. 11.** Intensity profile of the fundamental TE mode in the WG-QDPD. The cross section at position  $x = 0$  is shown in the right figure. Light is absorbed through the evanescent tail of the optical mode extended into the  $2.1 \mu\text{m}$  QD film.

layer on top were removed by immersing the sample in acetone for 1 h.

### 5. QDs deposition and patterning

The QD film was patterned using EBL and the lift-off method. The desired pattern was generated using  $400 \text{ nm}$  thick ARP672.08 e-beam resist and EBL. Then, QD stacks were spin-coated on top with the same procedure in Appendix C. The sacrificial e-beam resist and QDs on top were removed by immersing the sample in acetone for 10 min. PMMA has good chemical compatibility with the solvent involved (n-octane and methanol) in QDs deposition.

### 6. P-contact deposition and patterning

The P-contact was patterned using EBL and the lift-off method. The desired pattern was generated using a  $1 \mu\text{m}$  thick ARP672.08 e-beam resist and EBL. In this process, the e-beam resist baking was adjusted to  $60^\circ\text{C}$  for 5 min on the hotplate, deviating from the standard  $150^\circ\text{C}$  baking temperature. This modification aimed at protecting QDs and avoiding dark current degradation. A short

sonication step was incorporated at the end of e-beam resist development to ensure a clean interface between QDs and the P-contact metal. Subsequently, an  $80 \text{ nm}$  thick layer of Au was evaporated as the P-contact metal. The sacrificial e-beam resist and the layer of QDs on top were removed by immersing the sample in acetone for 30 min.

### APPENDIX E: WG-QDPD CHARACTERIZATION

For DC measurements, a  $2.1 \mu\text{m}$  laser ( $\text{Cr}^{2+}:\text{ZnS}$  laser, IPG Photonics) was coupled to a ZrF4 fiber and then further coupled to the WG-QDPD through a grating coupler. I-V curves were characterized with a source measure unit (Keithley 2400).

For AC measurements, the setup, as shown in Fig. 12, involved a  $1.55 \mu\text{m}$  laser (Santec 510) that was modulated by a Mach-Zehnder electro-optical modulator (EOM). The EOM was adjusted to its linear operation point, where applied radio frequency signals (SMT03, Rohde & Schwarz) were converted to optical intensity modulation. The modulated optical signals were amplified by an erbium-doped fiber amplifier (EDFA) and then coupled to the WG-QDPD through edge coupling. Polarization controllers (PC) were employed before

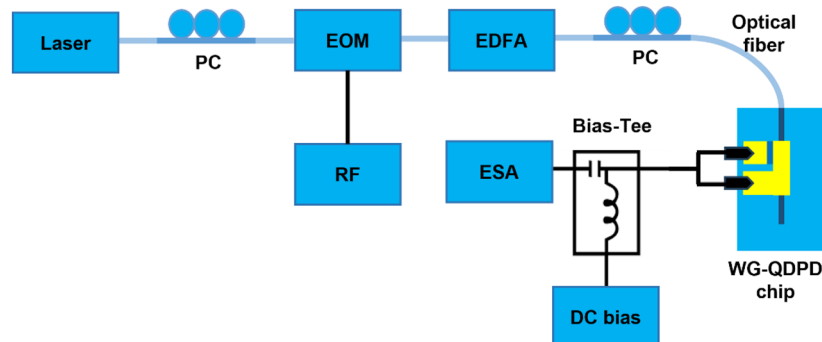


**FIG. 12.** Setup schematics used for bandwidth measurement. PC: polarization controller, EOM: electro-optical modulator, EDFA: erbium-doped fiber amplifier, RF: radio-frequency source, ESA: electrical spectrum analyzer.

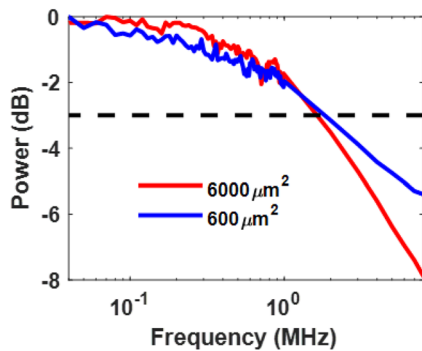


**FIG. 13.** Bandwidth of WG-QDPDs with different areas. WG-QDPDs, with a dimension of  $30\ \mu\text{m} \times 200\ \mu\text{m}$  and  $3\ \mu\text{m} \times 200\ \mu\text{m}$ , were measured under a reverse bias of  $-5\ \text{V}$ .

the EOM and our chip to achieve the desired polarization. A DC bias was applied to the WG-QDPD using a source measure unit (Keithley 2400). The photodetector signal was collected by an electrical spectrum analyzer (ESA, FSP, Rohde & Schwarz). Both the DC bias and ESA were connected to the WG-QDPD with a bias tee.

## REFERENCES

- M. Traverso, M. Mazzini, K. Lakshmi Kumar, S. Sunder, A. Kurylak, C. Appel, C. Muzio, R. Tummid, A. Cervasio, M. Nadeau, W. Li, J. Neiman, and M. Webster, "Integrated silicon photonics transceiver module for 100Gbit/s 20km transmission," in *Optics InfoBase Conference Papers* (Optica Publishing Group, formerly OSA, 2021).
- N. Margalit, C. Xiang, S. M. Bowers, A. Bjorlin, R. Blum, and J. E. Bowers, "Perspective on the future of silicon photonics and electronics," *Appl. Phys. Lett.* **118**(22), 220501 (2021).
- A. Z. Subramanian, E. Ryckeboer, A. Dhakal, F. Peyskens, A. Malik, B. Kuyken, H. Zhao, S. Pathak, A. Ruocco, A. De Groot, P. Wuytens, D. Martens, F. Leo, W. Xie, U. D. Dave, M. Muneeb, P. Van Dorpe, J. Van Campenhout, W. Bogaerts, P. Bienstman, N. Le Thomas, D. Van Thourhout, Z. Hens, G. Roelkens, and R. Baets, "Silicon and silicon nitride photonic circuits for spectroscopic sensing on-a-chip [Invited]," *Photonics Res.* **3**(5), B47 (2015).
- R. Wang, A. Vasiliev, M. Muneeb, A. Malik, S. Sprengel, G. Boehm, M.-C. Amann, I. Šimonytė, A. Vizbaras, K. Vizbaras, R. Baets, and G. Roelkens, "III-V-on-Silicon photonic integrated circuits for spectroscopic sensing in the 2–4  $\mu\text{m}$  wavelength range," *Sensors* **17**(8), 1788 (2017).
- T. Hu, B. Dong, X. Luo, T.-Y. Liow, J. Song, C. Lee, and G.-Q. Lo, "Silicon photonic platforms for mid-infrared applications [Invited]," *Photonics Res.* **5**(5), 417 (2017).
- E. Ryckeboer, A. Gassenq, M. Muneeb, N. Hattasan, S. Pathak, L. Cerutti, J. B. Rodriguez, E. Tournié, W. Bogaerts, R. Baets, and G. Roelkens, "Silicon-on-insulator spectrometers with integrated GaInAsSb photodiodes for wide-band spectroscopy from 1510 to 2300 nm," *Opt. Express* **21**(5), 6101–6108 (2013).
- N. Hattasan, A. Gassenq, L. Cerutti, J. B. Rodriguez, E. Tournié, and G. Roelkens, "Heterogeneous integration of GaInAsSb *p-i-n* photodiodes on a silicon-on-insulator waveguide circuit," *IEEE Photonics Technol. Lett.* **23**(23), 1760–1762 (2011).
- A. Gassenq, N. Hattasan, L. Cerutti, J. B. Rodriguez, E. Tournié, and G. Roelkens, "Study of evanescently-coupled and grating-assisted GaInAsSb photodiodes integrated on a silicon photonic chip," *Opt. Express* **20**(11), 11665 (2012).
- R. Wang, S. Sprengel, M. Muneeb, G. Boehm, R. Baets, M.-C. Amann, and G. Roelkens, "2  $\mu\text{m}$  wavelength range InP-based type-II quantum well photodiodes heterogeneously integrated on silicon photonic integrated circuits," *Opt. Express* **23**(20), 26834 (2015).
- M. Long, P. Wang, H. Fang, and W. Hu, "Progress, challenges, and opportunities for 2D material based photodetectors," *Adv. Funct. Mater.* **29**(19), 1803807 (2019).
- X. Wang, Z. Cheng, K. Xu, H. K. Tsang, and J. B. Xu, "High-responsivity graphene/silicon-heterostructure waveguide photodetectors," *Nat. Photonics* **7**(11), 888–891 (2013).
- J. Guo, J. Li, C. Liu, Y. Yin, W. Wang, Z. Ni, Z. Fu, H. Yu, Y. Xu, Y. Shi, Y. Ma, S. Gao, L. Tong, and D. Dai, "High-performance silicon-graphene hybrid plasmonic waveguide photodetectors beyond 1.55  $\mu\text{m}$ ," *Light: Sci. Appl.* **9**(1), 29 (2020).
- Y. H. Peng, H. H. Cheng, V. I. Mashanov, and G. E. Chang, "GeSn *p-i-n* waveguide photodetectors on silicon substrates," *Appl. Phys. Lett.* **105**(23), 231109 (2014).
- C.-H. Tsai, K.-C. Lin, C.-Y. Cheng, K.-C. Lee, H. H. Cheng, and G.-E. Chang, "GeSn lateral *p-i-n* waveguide photodetectors for mid-infrared integrated photonics," *Opt. Lett.* **46**(4), 864 (2021).
- S. Ghosh, R. Bansal, G. Sun, R. A. Soref, H. H. Cheng, and G. E. Chang, "Design and optimization of GeSn waveguide photodetectors for 2- $\mu\text{m}$  band silicon photonics," *Sensors* **22**(11), 3978 (2022).
- C.-H. Liu, R. Bansal, C.-W. Wu, Y.-T. Jheng, and G.-E. Chang, "GeSn waveguide photodetectors with vertical *p-i-n* heterostructure for integrated photonics in the 2  $\mu\text{m}$  wavelength band," *Adv. Photonics Res.* **3**(7), 2100330 (2022).
- J. Wu, Q. Jiang, S. Chen, M. Tang, Y. I. Mazur, Y. Maidaniuk, M. Benamara, M. P. Semtsiv, W. T. Masselink, K. A. Sablon, G. J. Salamo, and H. Liu, "Monolithically integrated InAs/GaAs quantum dot mid-infrared photodetectors on silicon substrates," *ACS Photonics* **3**(5), 749–753 (2016).
- G. H. Ahn, A. D. White, H. Kim, N. Higashitarumizu, F. M. Mayor, J. F. Herrmann, W. Jiang, K. K. S. Multani, A. H. Safavi-Naeini, A. Javey, and J. Vučković, "Platform-agnostic waveguide integration of high-speed photodetectors with evaporated tellurium thin films," *Optica* **10**(3), 349 (2023).
- J. Jean, J. Xiao, R. Nick, N. Moody, M. Nasilowski, M. Bawendi, and V. Bulović, "Synthesis cost dictates the commercial viability of lead sulfide and perovskite quantum dot photovoltaics," *Energy Environ. Sci.* **11**(9), 2295–2305 (2018).
- S. Lu, P. Liu, J. Yang, S. Liu, Y. Yang, L. Chen, J. Liu, Y. Liu, B. Wang, X. Lan, J. Zhang, L. Gao, and J. Tang, "High-performance colloidal quantum dot photodiodes via suppressing interface defects," *ACS Appl. Mater. Interfaces* **15**(9), 12061–12069 (2023).
- Y. Wang, H. Hu, M. Yuan, H. Xia, X. Zhang, J. Liu, J. Yang, S. Xu, Z. Shi, J. He, J. Zhang, L. Gao, J. Tang, and X. Lan, "Colloidal PbS quantum dot photodiode imager with suppressed dark current," *ACS Appl. Mater. Interfaces* **15**, 58573 (2023).
- D. H. Parmar, J. M. Pina, T. Zhu, M. Vafaie, O. Atan, M. Biondi, A. M. Najjariyan, S. Hoogland, and E. H. Sargent, "Controlled crystal plane orientations in the ZnO transport layer enable high-responsivity, low-dark-current infrared photodetectors," *Adv. Mater.* **34**(17), 2200321 (2022).
- M. Vafaie, J. Z. Fan, A. Morteza Najarian, O. Ouellette, L. K. Sagar, K. Bertens, B. Sun, F. P. Garcia de Arquer, and E. H. Sargent, "Colloidal quantum dot photodetectors with 10-ns response time and 80% quantum efficiency at 1,550 nm," *Matter* **4**(3), 1042–1053 (2021).
- J. Yang, H. Hu, Y. Lv, M. Yuan, B. Wang, Z. He, S. Chen, Y. Wang, Z. Hu, M. Yu, X. Zhang, J. He, J. Zhang, H. Liu, H. Y. Hsu, J. Tang, H. Song, and X. Lan, "Ligand-engineered HgTe colloidal quantum dot solids for infrared photodetectors," *Nano Lett.* **22**(8), 3465–3472 (2022).
- S. Keuleyan, E. Lhuillier, V. Brajuskovic, and P. Guyot-Sionnest, "Mid-infrared HgTe colloidal quantum dot photodetectors," *Nat. Photonics* **5**(8), 489–493 (2011).
- S. B. Hafiz, M. R. Scimeca, P. Zhao, I. J. Paredes, A. Sahu, and D. K. Ko, "Silver selenide colloidal quantum dots for mid-wavelength infrared photodetection," *ACS Appl. Nano Mater.* **2**(3), 1631–1636 (2019).
- S. B. Hafiz, M. M. Al Mahfuz, S. Lee, and D. K. Ko, "Midwavelength infrared *p-n* heterojunction diodes based on intraband colloidal quantum dots," *ACS Appl. Mater. Interfaces* **13**(41), 49043–49049 (2021).
- J. Leemans, V. Pejović, E. Georgitzikis, M. Minjauw, A. B. Siddik, Y. H. Deng, Y. Kuang, G. Roelkens, C. Detavernier, I. Lieberman, P. E. Malinowski, D. Cheyns,

- and Z. Hens, "Colloidal III–V quantum dot photodiodes for short-wave infrared photodetection," *Adv. Sci.* **9**(17), 2200844 (2022).
- <sup>29</sup>L. Elsinger, R. Petit, F. Van Acker, N. K. Zawacka, I. Tanghe, K. Neyts, C. Detavernier, P. Geiregat, Z. Hens, and D. Van Thourhout, "Waveguide-coupled colloidal quantum dot light emitting diodes and detectors on a silicon nitride platform," *Laser Photonics Rev.* **15**(7), 2000230 (2021).
- <sup>30</sup>W. Xie, Y. Zhu, S. Bisschop, T. Aubert, Z. Hens, D. Van Thourhout, and P. Geiregat, "Colloidal quantum dots enabling coherent light sources for integrated silicon-nitride photonics," *IEEE J. Sel. Top. Quantum Electron.* **23**(5), 1 (2017).
- <sup>31</sup>Y. Zhu, W. Xie, S. Bisschop, T. Aubert, E. Brainis, P. Geiregat, Z. Hens, and D. Van Thourhout, "On-chip single-mode distributed feedback colloidal quantum dot laser under nanosecond pumping," *ACS Photonics* **4**(10), 2446–2452 (2017).
- <sup>32</sup>W. Xie, T. Stöferle, G. Rainò, T. Aubert, S. Bisschop, Y. Zhu, R. F. Mahrt, P. Geiregat, E. Brainis, Z. Hens, and D. Van Thourhout, "On-chip integrated quantum-dot-silicon-nitride microdisk lasers," *Adv. Mater.* **29**(16), 1604866 (2017).
- <sup>33</sup>H. Jung, M. Lee, C. Han, Y. Park, K.-S. Cho, and H. Jeon, "Efficient on-chip integration of a colloidal quantum dot photonic crystal band-edge laser with a coplanar waveguide," *Opt. Express* **25**(26), 32919 (2017).
- <sup>34</sup>C. Pang, Y.-H. Deng, E. Kheradmand, N. Poonkottil, R. Petit, L. Elsinger, C. Detavernier, P. Geiregat, Z. Hens, and D. Van Thourhout, "Integrated PbS colloidal quantum dot photodiodes on silicon nitride waveguides," *ACS Photonics* **10**(12), 4215–4224 (2023).
- <sup>35</sup>B. Zhu, M. Chen, Q. Zhu, G. Zhou, N. M. Abdelazim, W. Zhou, S. V. Kershaw, A. L. Rogach, N. Zhao, and H. K. Tsang, "Integrated plasmonic infrared photodetector based on colloidal HgTe quantum dots," *Adv. Mater. Technol.* **4**(10), 1900354 (2019).
- <sup>36</sup>C. Dong, S. Liu, N. Barange, J. Lee, T. Pardue, X. Yi, S. Yin, and F. So, "Long-wavelength lead sulfide quantum dots sensing up to 2600 nm for short-wavelength infrared photodetectors," *ACS Appl. Mater. Interfaces* **11**(47), 44451–44457 (2019).
- <sup>37</sup>M. P. Hendricks, M. P. Campos, G. T. Cleveland, I. Jen-La Plante, and J. S. Owen, "A tunable library of substituted thiourea precursors to metal sulfide nanocrystals," *Science* **348**(6240), 1226–1230 (2015).
- <sup>38</sup>C. H. M. Chuang, P. R. Brown, V. Bulović, and M. G. Bawendi, "Improved performance and stability in quantum dot solar cells through band alignment engineering," *Nat. Mater.* **13**(8), 796–801 (2014).
- <sup>39</sup>S. Braun, W. R. Salaneck, and M. Fahlman, "Energy-level alignment at organic/metal and organic/organic interfaces," *Adv. Mater.* **21**(14–15), 1450–1472 (2009).
- <sup>40</sup>M. Biondi, M. J. Choi, O. Ouellette, S. W. Baek, P. Todorović, B. Sun, S. Lee, M. Wei, P. Li, A. R. Kirmani, L. K. Sagar, L. J. Richter, S. Hoogland, Z. H. Lu, F. P. García de Arquer, and E. H. Sargent, "A chemically orthogonal hole transport layer for efficient colloidal quantum dot solar cells," *Adv. Mater.* **32**(17), 1906199 (2020).
- <sup>41</sup>Y. Deng, C. Pang, E. Kheradmand, J. Leemans, J. Bai, M. Minjauw, J. Liu, K. Molkens, J. Beeckman, C. Detavernier, P. Geiregat, D. Van Thourhout, and Z. Hens, "Short-wave infrared colloidal QDs photodetector with nanosecond response times enabled by ultrathin absorber layers," *Adv. Mater.* (published online, 2024).
- <sup>42</sup>Q. Xu, L. Meng, K. Sinha, F. I. Chowdhury, J. Hu, and X. Wang, "Ultrafast colloidal quantum dot infrared photodiode," *ACS Photonics* **7**(5), 1297–1303 (2020).
- <sup>43</sup>I. Del Villar, C. R. Zamarreño, M. Hernaez, F. J. Arregui, and I. R. Matias, "Lossy mode resonance generation with indium-tin-oxide-coated optical fibers for sensing applications," *J. Lightwave Technol.* **28**(1), 111–117 (2010).
- <sup>44</sup>W. Bogaerts, Y. Li, S. Pathak, A. Ruocco, M. Fiers, A. Ribeiro, E. Lambert, and P. Dumon, "Integrated design for integrated photonics: From the physical to the circuit level and back," *Proc. SPIE* **8781**, 878102 (2013).
- <sup>45</sup>J. Brouckaert, W. Bogaerts, S. Selvaraja, P. Dumon, R. Baets, and D. Van Thourhout, "Planar concave grating demultiplexer with high reflective Bragg reflector facets," *IEEE Photonics Technol. Lett.* **20**(4), 309–311 (2008).
- <sup>46</sup>S. M. Koepfli, M. Baumann, Y. Koyaz, R. Gadola, A. Güngör, K. Keller, Y. Horst, S. Nashashibi, R. Schwanninger, M. Doderer, E. Passerini, Y. Fedoryshyn, and J. Leuthold, "Metamaterial graphene photodetector with bandwidth exceeding 500 gigahertz," *Science* **380**, 1169 (2023).
- <sup>47</sup>N. Youngblood, C. Chen, S. J. Koester, and M. Li, "Waveguide-integrated black phosphorus photodetector with high responsivity and low dark current," *Nat. Photonics* **9**(4), 247–252 (2015).
- <sup>48</sup>C. Liu, J. Guo, L. Yu, J. Li, M. Zhang, H. Li, Y. Shi, and D. Dai, "Silicon/2D-material photodetectors: From near-infrared to mid-infrared," *Light: Sci. Appl.* **10**(1), 123 (2021).
- <sup>49</sup>Y. Yin, R. Cao, J. Guo, C. Liu, J. Li, X. Feng, H. Wang, W. Du, A. Qadir, H. Zhang, Y. Ma, S. Gao, Y. Xu, Y. Shi, L. Tong, and D. Dai, "High-speed and high-responsivity hybrid silicon/black-phosphorus waveguide photodetectors at 2  $\mu\text{m}$ ," *Laser Photonics Rev.* **13**(6), 1900032 (2019).
- <sup>50</sup>X. Gan, R. J. Shiu, Y. Gao, I. Meric, T. F. Heinz, K. Shepard, J. Hone, S. Assefa, and D. Englund, "Chip-integrated ultrafast graphene photodetector with high responsivity," *Nat. Photonics* **7**(11), 883–887 (2013).
- <sup>51</sup>T. He, H. Ma, Z. Wang, Q. Li, S. Liu, S. Duan, T. Xu, J. Wang, H. Wu, F. Zhong, Y. Ye, J. Wu, S. Lin, K. Zhang, P. Martyniuk, A. Rogalski, P. Wang, L. Li, H. Lin, and W. Hu, "On-chip optoelectronic logic gates operating in the telecom band," *Nat. Photonics* **18**(1), 60–67 (2024).
- <sup>52</sup>T. Mueller, F. Xia, and P. Avouris, "Graphene photodetectors for high-speed optical communications," *Nat. Photonics* **4**(5), 297–301 (2010).
- <sup>53</sup>E. Lhuillier, S. Keuleyan, and P. Guyot-Sionnest, "Optical properties of HgTe colloidal quantum dots," *Nanotechnology* **23**(17), 175705 (2012).
- <sup>54</sup>M. M. Ackerman, X. Tang, and P. Guyot-Sionnest, "Fast and sensitive colloidal quantum dot mid-wave infrared photodetectors," *ACS Nano* **12**(7), 7264–7271 (2018).